







PAPER

# A 3D dynamic model to assess the impacts of low-mode asymmetry, aneurysms and mix-induced radiative loss on capsule performance across inertial confinement fusion platforms

To cite this article: P.T. Springer *et al* 2019 *Nucl. Fusion* **59** 032009

View the [article online](#) for updates and enhancements.

# A 3D dynamic model to assess the impacts of low-mode asymmetry, aneurysms and mix-induced radiative loss on capsule performance across inertial confinement fusion platforms

P.T. Springer<sup>1</sup>, O.A. Hurricane<sup>1</sup> , J.H. Hammer<sup>1</sup>, R. Betti<sup>3</sup>, D.A. Callahan<sup>1</sup>, E.M. Campbell<sup>3</sup>, D.T. Casey<sup>1</sup>, C.J. Cerjan<sup>1</sup>, D. Cao<sup>3</sup>, E. Dewald<sup>1</sup>, L. Divol<sup>1</sup>, T. Doeppner<sup>1</sup>, M.J. Edwards<sup>1</sup>, J.E. Field<sup>1</sup> , C. Forrest<sup>3</sup>, J. Frenje<sup>4</sup> , J.A. Gaffney<sup>1</sup>, M. Gatu-Johnson<sup>4</sup>, V. Glebov<sup>3</sup>, V.N. Goncharov<sup>3</sup>, G.P. Grim<sup>1</sup>, E. Hartouni<sup>1</sup>, R. Hatarik<sup>1</sup>, D.E. Hinkel<sup>1</sup>, L. Berzak Hopkins<sup>1</sup> , I. Igumenshchev<sup>3</sup>, P. Knapp<sup>2</sup>, J.P. Knauer<sup>3</sup>, A.L. Kritcher<sup>1</sup>, O. Landen<sup>1</sup>, A. Pak<sup>1</sup>, S. Le Pape<sup>1</sup>, T. Ma<sup>1</sup>, A.G. MacPhee<sup>1</sup>, D.H. Munro<sup>1</sup> , R.C. Nora<sup>1</sup>, P.K. Patel<sup>1</sup>, L. Peterson<sup>1</sup>, P.B. Radha<sup>3</sup>, S.P. Regan<sup>3</sup>, H. Rinderknecht<sup>1,3</sup> , C. Sangster<sup>3</sup>, B.K. Spears<sup>1</sup> and C. Stoeckl<sup>3</sup>

<sup>1</sup> Lawrence Livermore National Laboratory, Livermore, California, United States of America

<sup>2</sup> Sandia National Laboratory, Albuquerque, New Mexico, United States of America

<sup>3</sup> Laboratory for Laser Energetics, University of Rochester, Rochester, New York, United States of America

<sup>4</sup> Massachusetts Institute of Technology, Cambridge, Massachusetts, United States of America

E-mail: [springer6@llnl.gov](mailto:springer6@llnl.gov)

Received 19 July 2018, revised 30 October 2018

Accepted for publication 1 November 2018

Published 18 December 2018



## Abstract

A simple 3D dynamic model for inertial confinement fusion (ICF) implosions has been developed and used to assess the impacts of low-mode asymmetry, aneurysms and mix-induced radiative loss on capsule performance across ICF platforms. The model, while benchmarked against radiation hydrodynamics simulations, benefits from simplicity and speed to allow rapid assessment of possible sources of degradation as well as to help build intuition about the relative importance of different effects. Degradations in the model result from 3D  $\rho r$  areal density perturbations that grow under deceleration from a radial stagnation flow, resulting in reduced convergence, stagnation pressure and temperature. When available, experimental data are used as input to seed 3D perturbations in the model so that the actual observed hotspot and shell  $\rho r$  areal density asymmetry at stagnation, as well as the radiation loss increase from mix impurities, are accurately reproduced. This model is applied to a broad set of implosion data from the NIF and Omega, including examples from both indirect drive and direct drive. The model matches most experimental observables and explains major performance degradation mechanisms which can result in 30–100-fold reductions in yield. We examine a modified ignition criterion that accounts for the increase in expansion  $PdV$  work, due to the presence of 3D  $\rho r$  perturbations and loss-of-confinement in thin regions of the shell.

Keywords: inertial confinement fusion, ignition criterion, fuel assembly, low-mode asymmetry

(Some figures may appear in colour only in the online journal)

## 1. Introduction

Nuckolls *et al* claimed in their seminal paper 46 years ago:

‘Hydrogen may be compressed to more than 10 000 times liquid density by an implosion system energized by a high energy laser. This scheme makes possible efficient thermonuclear burn of small pellets of heavy hydrogen isotopes, and makes feasible fusion power reactors using practical lasers [1].’

Ignition requires precisely controlled, high convergence implosions to assemble a dense shell of deuterium–tritium (DT) fuel with  $\rho r > \sim 1 \text{ g cm}^{-2}$  surrounding a 10 keV hot spot with  $\rho r \sim 0.3 \text{ g cm}^{-2}$  [2–5]. Achieving these conditions requires that the self-heating of the plasma by alpha particle production from fusion reactions within the assembled hotspot of the implosion exceeds the losses from electron thermal conduction, x-ray radiation emission and hydrodynamic disassembly. Ignition is a threshold phenomenon, requiring a high enough starting pressure, temperature and size (or time) to begin the self-heating process, which will then further increase pressure, temperature and reaction rate, quickly reaching a runaway solution. When achieved, ignition is obvious, because the large neutron yield and associated energy production will greatly exceed the initial kinetic energy needed for the fuel assembly. When ignition does not occur, the difficulty is to figure out exactly why it did not, and what the most important changes needed to improve the margin are, namely the degree to which imperfections, mix, asymmetry, etc can be tolerated in the implosion and still ignite [6].

To achieve this goal, we need a 3D model of implosions that accounts for the major degradation mechanisms observed in experiments, and the ability to isolate the most important ones. While we do have high-fidelity 3D simulation [7, 8], runtimes are  $\sim 1$  month on 1000-processor supercomputers, and when completed are only as good as the inputs, and so may possibly disagree with important aspects of the data. While simulations play an important role in guiding experiments, they are often not predictive. We have simulations (particularly in 1D and 2D) that predict that a target should ignite and give high yield but that underperform in reality [9]. Why is this? Do the simulations have the right inputs, physical models, resolution and so on? We sometimes see unexplained emission from the hotspot, or  $\rho r$  asymmetry in an imploded core, showing 3D asymmetry much larger than model predictions. We see evidence of impacts of engineering features such as the fill tube and tent [10], and often observe lower  $\rho r$  and compression than predicted. What are the relative impacts of each, and what do we need to improve? It would be desirable if the 3D model were designed to explicitly agree with experimental data, perhaps using them as input, and to run a million times faster than the high-fidelity 3D simulations, so that models can be iterated quickly and used to provide timely feedback to the program experiments, as well as providing guidance for improving inputs to the high-fidelity simulations.

To this end, we have developed a 3D dynamic implosion model to assess the impacts of low-mode asymmetry and

‘loss-of-confinement’ [11] on performance (due to low  $\rho r$  regions in an imploding shell), as well as increased radiative loss due to impurities that are injected or mixed into the hotspot. The model is designed for speed (a few minutes runtime on a laptop) and flexibility, and accounts for the known processes of alpha heating, radiative loss, conduction and mass ablation into the hotspot, as well as the cold fuel stagnation and flow due to shape errors and mistiming of the stagnating elements. The goal of the model is to capture the state and  $\rho r$  asymmetries in the stagnated fuel, and associated degradations in performance. The model is initialized with  $\rho r$  and shape perturbations in the fuel that grow as expected in first order due to the physics of radial stagnation flow. The perturbations are chosen to match experimental observables at stagnation, such as the observed radiative loss and low-mode asymmetry observed in diagnostics such as neutron spectrometers and nuclear activation detectors that are sensitive to fuel  $\rho r$  asymmetry. We examine low-mode asymmetry and tent aneurysm leaks for the 20-shot high-foot series on the National Ignition Facility (NIF), which limits yields to  $\leq 1 \times 10^{16}$  and produces a performance cliff at high velocity. The impact of large  $m$ -mode asymmetries observed in the high yield high-density-carbon (HDC) diamond ablator implosions at the NIF are also examined, as well as possible stagnation pressure degradations in the University of Rochester’s Omega laser implosions due to the mounting stalk. We examine a modified ignition criterion that accounts for the increase in expansion  $PdV$  (pressure times change in volume) work due to the presence of 3D  $\rho r$  perturbations and loss-of-confinement in thin regions of the shell.

## 2. Overview

The body of this paper, following the introduction and overview, is comprised of five sections describing the model and application to data. Section 3 is a description of the dynamic model for the hotspot during the deceleration phase of the implosion, where the temperature, pressure and energy (volume) respond to the mechanical  $PdV$  work on the hotspot from the shell. Models for alpha particle production from fusion reactions and stopping, radiation loss from bremsstrahlung and impurity ions, and thermal conduction and mass ablation within the hotspot are important to the evolution of the pressure, temperature and 3D volume. These models must account for the temperature gradients inherent to the hotspot, even if the hotspot is treated as a single macro-zone (in 1D) or as multiple angular zones with a 3D faceted boundary.

Section 4 is a description of the dynamic model for the cold fuel that develops as a response to the pressure exerted by the hotspot. Key to this is a self-consistent solution to the Euler equations assuming uniform deceleration within the stagnated fuel in a zonal element. As a function of polar and azimuthal angles  $\theta$  and  $\varphi$ , the shell is characterized by five variables: the inner (hotspot) radius ( $r_{\text{hs}}$ ), the outer (shock) radius ( $r_s$ ), the inner (hotspot) pressure ( $P_{\text{hs}}$ ), the outer (shock) pressure ( $P_s$ ) and the accumulated mass ( $m$ ). At the shock position, Hugoniot conditions are used to determine the shock speed

relative to the infalling mass. The mass and pressure gradient within the stagnated shell are used to determine the deceleration of the shell, and thus the  $PdV$  work. The inputs are the density ( $\rho$ ), adiabat ( $\alpha$ ) and implosion velocity ( $v_{\text{imp}}$ ) of the infalling mass.

Section 5 discusses the 3D model, in which the shell is broken into multiple facets that are coupled by a common isobaric hotspot under the assumption of radial stagnation flow. The model is initiated by starting the implosion with a small amplitude, and 3D seed variation. The values of the ‘seed’ perturbations are chosen to reproduce the  $\rho r$  asymmetry at stagnation, as well as the radiative loss, that are both derived from data. Seeds could be in radius ( $\theta, \varphi$ ), velocity ( $\theta, \varphi$ ) or mass ( $\theta, \varphi$ ). Distortions grow because of the dependence of the deceleration on  $\frac{P}{\rho r}$ , because high  $\rho r$  regions are not effectively slowed by the hotspot, and low  $\rho r$  regions rebound early and expand by minimum volume. The model is tested against 2D radhydro simulations and compares well when seeds match the  $\rho r$  asymmetry at stagnation even when the distortions are large (a factor of two in shape, and of four in  $\rho r$ ). It is expected to work best for low-modes which tend to be the greatest source of degradation, particularly mode 1 [12].

Section 6 is a description of the application of the 3D model to data. The model matches most experimental observables and explains major performance degradation mechanisms which can be 30–100 in yield. Finally, section 7 examines a modified ignition criterion that accounts for the increase in expansion  $PdV$  work due to the presence of 3D  $\rho r$  perturbations and loss-of-confinement in thin regions of the shell. The modified criterion is based on requiring the first and second derivative of hotspot temperature to be positive at minimum volume [13], when the  $PdV$  work term in expansion starts to be a drain on the alpha heating. This can be evaluated analytically from the equations for hotspot heating at minimum volume and is equivalent to requiring a higher temperature ( $\sim 5.5$  keV) for NIF implosions. For high enough  $\rho r$  that are also close to 1D, the second derivative term is usually easily satisfied—it is not in play. For  $\rho r < 1$  g cm $^{-2}$  with observed asymmetry, and aneurysms, the NIF implosions tend to fail in the regime where  $\frac{d^2T}{dr^2} < 0$ , and expansion cooling dominates. We compare the modified ignition criterion to an ensemble of 60000 ICF implosion simulations made at the Los Alamos National Laboratory (LANL) Trinity supercomputer and find that implosions which have  $\frac{d^2T}{dr^2} < 0$  always fail to ignite, and that this regime is under-sampled in ensemble simulations. An improved version of the 3D ignition criterion based on a general explosion solution to the pressure equation, including nonradial flows, will be reported elsewhere, but agrees with the first and second derivative of temperature approximation for conventional implosions.

### 3. Dynamic model for the hotspot

The hotspot is initially formed from shock heating of the low density central vapor, which initially rises to a much higher temperature than the surrounding concentric DT ice layer. The

model starts during the deceleration phase of the implosion when the shock heating has thermalized, and for simplicity we assume equilibrium between electron and ion temperatures. Subsequent mechanical or  $PdV$  work on the hotspot will further increase temperature until heat conduction dominates the energy flow in the incipient hotspot. The model contains a central isobaric hotspot, meaning it has the same time dependent pressure throughout the hotspot volume. The isobaric approximation is valid in the hotspot because the flow velocity (typically  $\sim 100$  km s $^{-1}$ ) is much lower than the sound speed ( $\sim 600$  km s $^{-1}$ ) in the hotspot, and the associated pressure drop is a small fraction of the hotspot pressure  $\sim \left(\frac{v_{\text{flow}}}{v_{\text{sound}}}\right)^2$ . The hotspot is presumed to have a temperature profile that is hot in the middle and cold at the boundary. Because of the temperature gradients within the hotspot, heat will flow out of the hotspot. The heat flow is a strong function of thermal temperature  $\sim T^{7/2}$  for Spitzer conductivities, so heat conduction will limit the hotspot temperature by ablation of cold fuel at the hotspot edge into the hotspot. A simple model for this process, developed by Betti [14], is obtained by considering the ‘hotspot’ to be comprised of a central hot volume surrounded by a much smaller volume of dense fuel. The dense outer boundary contains enough mass to feed the mass ablation by conduction into the hotspot, while remaining cold enough that conductive heat flow at the boundary can be neglected. The hotspot is then adiabatic and  $PV^\gamma$  is conserved for the hotspot with its cold dense boundary as mechanical work from the shell compresses and heats the hotspot. We use an ideal gas law value for the ratio of the specific heats at constant pressure and constant volume  $\gamma = \frac{C_p}{C_v} = \frac{5}{3}$ . With corrections for alpha heating and radiative loss, the pressure can be related simply to the mechanical work done on the hotspot. Furthermore, the heat flow within the hotspot and mass ablation into the hotspot, which determines the hotspot temperature, has no direct impact on the hotspot pressure or energy.

A key approximation in the model is that the hotspot is isobaric and has a conduction-dominated temperature profile. This allows for the use of simple formulas for the rates of alpha heating, and the radiative and conductive cooling that depend only on the pressure, central temperature and radius (in 1D). The temperature profile is the steady state solution to the heat flow equation, and is isobaric, in spite of alpha heating, radiative loss and mass ablation. These are good approximations in comparison to simulation. In this case, there is a characteristic temperature profile obtained by solving the heat flow equation

$$\rho C_p \frac{dT}{dt} = C_p \frac{P}{T} \frac{dT}{dt} = \nabla \cdot (K \vec{\nabla} T) = q \quad (1)$$

in which the left-hand side represents the time rate of change of the energy per unit volume. Solutions are found for the temperature as a product  $T_{\text{hs}}(r, t) = T_o(t) F(\vec{r})$  so that the heating rate which depends on  $\frac{P}{T} \frac{dT}{dt}$  depends on time but not space. The right-hand side of the heating equation is the divergence of the heat flux within the hotspot, where the heat flux is the product of thermal conductivity  $K$  and the gradient in temperature  $T$ ,  $C_p$  is the specific heat at constant pressure, and

$q$  represents the volumetric heating rate that depends on time but not space. Typically, the thermal conductivity  $K$  is a strong function of temperature

$$K = k_0 T^\beta \quad (2)$$

where  $k_0$  is a constant, and the temperature exponent  $\beta$  is typically  $\sim 2.0$ – $2.5$ .

The heat flow equation has solutions for  $T^{\beta+1}$  that are quadratic in space, and the boundary condition that the temperature approaches zero at the outer boundary leads to characteristic solutions

$$T_{\text{hs}}(r, t) = T_0(t) \left(1 - \left(\frac{r}{R}\right)^2\right)^{\frac{1}{1+\beta}} \quad (3)$$

for spherical hotspots or

$$T_{\text{hs}}(x, y, z, t) = T_0(t) \left(1 - \left(\frac{x}{x_0}\right)^2 - \left(\frac{y}{y_0}\right)^2 - \left(\frac{z}{z_0}\right)^2\right)^{\frac{1}{1+\beta}} \quad (4)$$

for an ellipsoidal solution with axial distance parameters  $(x_0, y_0, z_0)$  where  $T_0$  is the central temperature. The total heat flow is given by

$$Q_{\text{cond}} = \frac{8\pi}{3} \frac{1}{1+\beta} K T_0 x_0 y_0 z_0 \left(\frac{1}{x_0^2} + \frac{1}{y_0^2} + \frac{1}{z_0^2}\right). \quad (5)$$

For a given volume the conduction losses are minimized for a spherical implosion, but even when the hotspot is oblate or prolate with an elliptical aspect ratio as large as two, the conduction losses only increase about 20%. For the thermal conductivity we use a fit to the Sesame database for DT.

$$K = 3.21 \times 10^{13} \left(\frac{\rho}{80}\right)^{0.194} \left(\frac{T}{2.5}\right)^{2.21} \frac{\text{W}}{\text{cm keV}} \quad (\beta = 2.21 - 0.194 = 2.016). \quad (6)$$

The ideal gas law for hot DT for pressure in Gbar, density in  $\text{g cm}^{-3}$ , and temperature in keV:

$$P = 0.77 \rho T. \quad (7)$$

With a known pressure, central temperature and radial temperature profile, the alpha heating, radiative loss and conductive cooling rates can be calculated using the appropriate nuclear, atomic and transport data. Neutron production and alpha heating rates were calculated using the Caughlan and Fowler DTn cross-sections and then fit to a functional form. DCA opacities and emissivities for DT were used to calculate the radiative loss rates, including the reduction in radiative loss due to reabsorption in the hotspot. Even with an irregular 3D hotspot boundary, the alpha heating and radiative loss both scale as  $P^2V$  but have different dependencies on temperature. This simplification allows the hotspot to be treated as a single zone in a 1D model, and as slices of a 1D solution in a 3D model because the ellipsoidal solution has the same radial profile as the spherical case, with corrections for conduction loss in formula (5).

Neutron production rates, which scale as  $P^2V$ , were calculated for the hotspot using the nuclear cross-sections of Caughlan and Fowler [15] over a temperature range from 1–20 keV, and fit to the following form:

$$\frac{dN}{dt}(P, R, T) = 1 \times 10^{10} \left(\frac{P_{\text{hs}}}{202.8}\right)^2 \left(\frac{R}{0.004}\right)^3 \times \exp \left[38.091 - 2.2523 \times \exp\left(\frac{1-T}{0.68238}\right) - 4.265 \times \exp\left(\frac{1-T}{4.1743}\right)\right]. \quad (8)$$

In these expressions  $P$  is in Gbar,  $R$  in cm, and  $T$  in keV. The alpha heating rate, assuming the 3.5 MeV/alpha stops within the adiabatic hotspot including the cold outer boundary, is then:

$$Q_\alpha = \frac{dN}{dt}(P, R, T) \times 3.5 \times 10^6 \times 1.6 \times 10^{-19} \text{ W}. \quad (9)$$

The portion that stops within the hot region of the hotspot is denoted  $f_\alpha$  and uses the alpha stopping model of Krokhin and Rosanov [16].  $f_\alpha > 0.8$  for the temperature and hotspot  $\rho r$  typical of NIF implosions at bang time.

$$f_\alpha = 1 - \frac{1}{4\psi} + \frac{1}{160\psi^3} : \psi = \frac{\rho r_{\text{hs}} (1 + 0.0082 T)^{1.25}}{0.025 T^{1.25}}. \quad (10)$$

The radiative loss rates for an optically thin hotspot, which also scale as  $P^2V$ , were calculated using non-local thermodynamic opacity tables for DT using the DCA model of Howard Scott [17], and fit to the following form:

$$Q_{\text{rad}} = 4.24 \times 10^{14} \left(\frac{P_{\text{hs}}}{202.8}\right)^2 \left(\frac{R}{0.004}\right)^3 T^{-1.3023} \text{ W}. \quad (11)$$

This radiative loss is reduced by a factor of approximately two due to reabsorption of x-rays below  $\sim 2$  keV photon energy given typical values of temperature and hotspot  $\rho r$ . The reabsorption of x-rays within the hotspot was calculated using the DCA opacity model to calculate the escape probability versus hotspot  $\rho r$  and photon energy. With models for the alpha heating, the fractional stopping inside the cold boundary, the conduction losses (that ablate mass into the hotspot) and the radiative loss, we can construct equations to determine the hotspot pressure and temperature as a function of time:

$$\frac{dP_{\text{hs}}}{dt} = \frac{P_{\text{hs}}}{E_{\text{hs}}} \left(Q_\alpha - Q_{\text{rad}} - \frac{5}{2} P_{\text{hs}} \frac{dV}{dt}\right), \quad (12)$$

$$\frac{dT_{\text{hs}}}{dt} = \frac{T_{\text{hs}}}{E_{\text{hs}}} \left(f_\alpha Q_\alpha - Q_{\text{rad}} - Q_{\text{cond}} - P_{\text{hs}} \frac{dV}{dt}\right), \text{ and} \quad (13)$$

$$E_{\text{hs}} = \frac{3}{2} P_{\text{hs}} V. \quad (14)$$

The hotspot model would be complete if we had a model for the  $PdV$  work of the shell upon the hotspot, or alternatively the hotspot volume versus time. For this we need to examine the work done on the hotspot by the stagnating fuel.

#### 4. Dynamic model for the stagnation of the cold fuel

The deceleration phase of the implosion begins when the hotspot pressure exceeds the pressure of the infalling fuel. This causes the formation of a compression sound wave and, eventually, a shock wave that travels back upstream into the infalling fuel. As fuel crosses the stagnation shock, the mass and thickness of the shocked region increases, and a pressure gradient between the hotspot and shock pressure develops in

time. The hotspot dynamics depend upon its deceleration, which is determined by this pressure gradient in the stagnated fuel. We use a model that is a self-consistent solution to the Euler equations assuming uniform deceleration within the stagnated fuel in a zonal element. At the shock position, Hugoniot conditions are used to determine the shock speed  $u$  relative to the infalling mass. The mass and pressure gradient within the stagnated shell are then used to determine the deceleration of the shell, and thus the  $PdV$  work.

We suppose that the stagnated fuel has an adiabat  $\alpha_s$ , which we assume is uniform throughout the volume. We expect  $\alpha_s$  to be higher than the inflight adiabat because of the slight heating from the stagnation shock [18] and mostly by the reabsorption of radiation that escapes the hotspot, and the value of  $\alpha_s$  is adjusted to conserve energy deposited in the stagnated fuel. We also assume a uniform deceleration of the stagnated fuel given by  $\ddot{r}_{hs} = g$ , which depends on time but not radial position inside the stagnated fuel. The relationship between pressure and density in the stagnated fuel is given by

$$P = 4 \times 10^{15} \alpha_s \left( \frac{\rho}{100} \right)^\gamma \quad (\text{cgs units} \rightarrow 1 \times 10^{15} \text{ cm cm}^{-3} = 1 \text{ Gbar}). \quad (15)$$

And so, the force equation assuming a uniform deceleration  $g$  determines

$$\frac{\partial P}{\partial r} = -\rho g = \gamma 4 \times 10^{15} \alpha_s \frac{\rho^{\gamma-1}}{100^\gamma} \frac{\partial \rho}{\partial r}, \quad (16)$$

which is integrated and solved to give the radial density profile

$$\rho = \rho_{\max} \left( 1 - \left( \frac{\gamma-1}{\gamma} \right) \frac{g 100^\gamma}{4 \times 10^{15} \alpha_s \rho_{\max}^{\gamma-1}} (r - r_{hs}) \right)^{\frac{1}{\gamma-1}}, \quad \text{with} \quad (17)$$

$$\rho_{\max} = 100 \left( \frac{P_{hs}}{4 \times 10^{15} \alpha_s} \right)^{1/\gamma} \quad (18)$$

and the radial pressure profile

$$P = P_{hs} \left( 1 - \left( \frac{\gamma-1}{\gamma} \right) \frac{g \rho_{\max}}{P_{hs}} (r - r_{hs}) \right)^{\frac{\gamma}{\gamma-1}} \quad (19)$$

from which we can determine the ratio  $\frac{P_s}{P_{hs}}$

$$\frac{P_s}{P_{hs}} = \left( 1 - \left( \frac{\gamma-1}{\gamma} \right) \frac{g \rho_{\max}}{P_{hs}} (r_s - r_{hs}) \right)^{\frac{\gamma}{\gamma-1}}. \quad (20)$$

The force equation also gives a relationship between pressure drop and shell  $\rho r$ , which allows us to relate  $g$  to the accumulated mass

$$\ddot{r}_{hs} = g = \frac{(P_{hs} - P_s) 4\pi \bar{r}^2}{m} \quad (21)$$

where the mass  $m$  is

$$m = \int_{r_{hs}}^{r_s} 4\pi \rho r^2 dr \quad (22)$$

and

$$\bar{r}^2 = \frac{\int_{r_{hs}}^{r_s} \rho r^2 dr}{\int_{r_{hs}}^{r_s} \rho dr} r_{hs} < \bar{r} < r_s \quad (23)$$

so

$$\frac{P_s}{P_{hs}} = \left( 1 - \left( \frac{\gamma-1}{\gamma} \right) \frac{(P_{hs} - P_s) 4\pi \bar{r}^2}{m} \frac{\rho_{\max}}{P_{hs}} (r_s - r_{hs}) \right)^{\frac{\gamma}{\gamma-1}} \quad (24)$$

and

$$\frac{1 - \left( \frac{P_s}{P_{hs}} \right)^{\frac{\gamma-1}{\gamma}}}{1 - \left( \frac{P_s}{P_{hs}} \right)} = \left( \frac{\gamma-1}{\gamma} \right) \rho_{\max} \frac{4\pi \bar{r}^2}{m} (r_s - r_{hs}) \equiv f. \quad (25)$$

For a given value of the dimensionless profile factor  $f$  this equation can be inverted for  $\gamma = \frac{5}{3}$  approximately by

$$\begin{aligned} P_s &= P_{hs} \left[ (1-f)^{2.5} + 9.274 (1-f)^5 \right] \quad (0.4 < f \lesssim 1.0) \\ P_s &= P_{hs} \quad f < 0.4 \\ P_s &= P_i \quad f \gtrsim 1.0 \end{aligned} \quad (26)$$

where  $P_i$ ,  $\rho_i$ , and  $v_{\text{imp}}$  are determined from the cold fuel adiabat, velocity and convergence radius. As  $f \rightarrow 1$  we must limit the shock pressure  $P_s$  to be greater or equal to the infalling pressure  $P_i$ . The shock speed  $u$  needed to obtain the shock pressure  $P_s$  is obtained from Hugoniot relations,

$$u = \left( \frac{P_i}{\rho_i} \frac{2\gamma}{(\gamma+1) \frac{\rho_i}{\rho_s} - (\gamma-1)} \right)^{\frac{1}{2}} \quad (27)$$

and

$$\frac{\rho_s}{\rho_i} = \frac{(\gamma+1) \frac{P_s}{P_i} + (\gamma-1)}{(\gamma+1) + (\gamma-1) \frac{P_s}{P_i}}. \quad (28)$$

The shock speed in turn determines the evolution of the shock position from the shock characteristic

$$\dot{r}_s = -v_{\text{imp}} + u \quad (29)$$

and the mass accumulation rate

$$\frac{\partial m}{\partial t} = 4\pi r_s^2 \rho_i u. \quad (30)$$

The 3D model time dependent hotspot and shock radii are also functions of polar and azimuthal angle,  $r_{hs}(\theta, \varphi, t)$  and  $r_s(\theta, \varphi, t)$ , with hotspot volume  $V = \frac{1}{3} \int r_{hs}(\theta, \varphi, t)^3 d\Omega$  and with the radii evolving according to the equations above for each facet, which share a common hotspot.

## 5. Construction of 3D dynamic model

In a symmetric implosion each facet of the shell has the same  $\rho r$  as a function of time, and each facet arrives at minimum volume at the same time, so that  $\partial KE / \partial t$ , pressure, and  $PV$  energy are maximized. As the hotspot reaches its minimum volume and begins to expand, almost all of the kinetic energy of the stagnated fuel has gone into compression, and the alpha heating rates relative to conduction and radiative loss rates are maximized if temperature is high enough. In experiments, however, we observe large  $\rho r$  variations of the stagnated fuel,

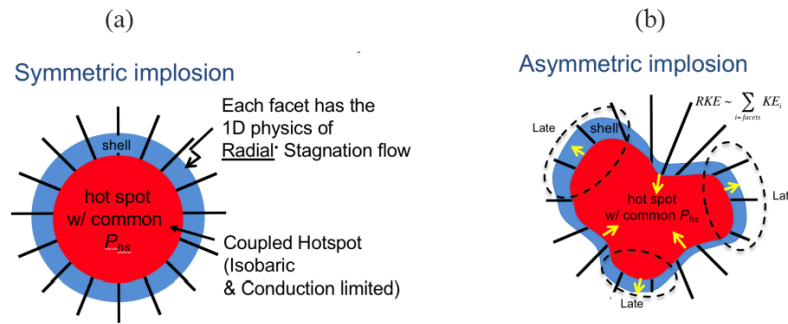


**Figure 1.** The 3D model breaks the shell into facets and treats the work of each facet as a radial stagnation upon a common isobaric and conduction limited hotspot, accounting for conduction, alpha heating and radiation loss. In a symmetric implosion (a) each facet of the shell has the same  $\rho r$  and arrives at minimum volume at the same time so  $d(KE)/dt$ , pressure and  $PV$  energy are maximized. In an asymmetric implosion (b) late and low  $\rho r$  facets of the shell rebound before minimum volume, leaving residual kinetic energy RKE and reduced  $d(KE)/dt$ , pressure and  $PV$  energy.

often with more than twice the variation in  $\rho r$  and often with large  $m$ -mode components that are orthogonal to the hohlraum axis of symmetry. These are manifested in variations in the uniformity of unscattered, 14 MeV neutrons with polar and azimuthal angles measured in the flange nuclear activation detectors (FNADs), and also in a corresponding residual velocity of the hotspot measured in the neutron time-of-flight (NTOF) detectors, that tends to flow from the high  $\rho r$  regions and towards the low  $\rho r$  regions. These asymmetries result from percent-level flux asymmetries in the hohlraum drive.

As illustrated in figure 1, we model the asynchronous stagnation of asymmetric shell elements by breaking the 3D implosion into facets and treating each facet with the 1D physics of radial stagnation flow. Each facet does work upon a common hotspot that is treated as isobaric and conduction limited. The approximation of radial flow greatly simplifies the model and is valid for the lowest modes where the curvature of the hotspot is close to 1D. Kritcher [19] showed that even simulations of highly distorted implosions having significant  $\rho r$  variation had mainly radial flow. At bang time, the residual kinetic energy (RKE) was mostly due to radial motion, and the nonradial kinetic energy was less than 1% of the total kinetic energy. Assuming a uniform mass  $sr^{-1}$  and uniform initial velocity, portions of the shell that lead the stagnation (coming in early) will have a higher  $\rho r$  (due to the higher convergence) and a smaller acceleration. Likewise, late and low  $\rho r$  facets of the shell will have a lower  $\rho r$  and higher acceleration, and will rebound before minimum volume. The time rate of change of the hotspot volume  $\frac{\partial V}{\partial t} = \int r^2 \dot{r} d\Omega$  is zero at minimum volume and the shell is comprised of high  $\rho r$  regions still converging to the center ( $\dot{r} < 0$ ), and low  $\rho r$  regions that have rebounded early ( $\dot{r} > 0$ ), resulting in RKE, reduced  $\frac{\partial(KE)}{\partial t}$ , pressure and  $PV$  energy.

The 3D dynamic model compares well to detailed radhydro simulations using an ellipsoidal perturbation that was varied from highly oblate to prolate. The results are displayed in figure 2. Yield variations of a factor of ten were predicted, and the 3D dynamic model matched these as the elliptical aspect ratio at bang time was varied from two times sausage to two times pancaked (by a factor of two in shape, and of four in  $\rho r$ ), providing the elliptical aspect ratio at bang time was

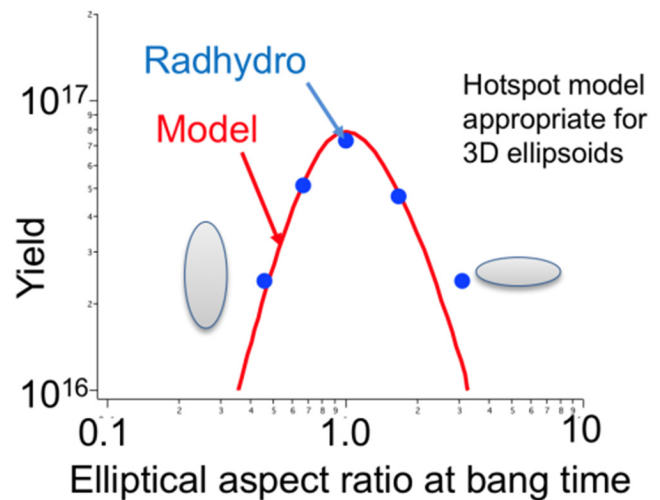


**Figure 2.** 3D dynamic model (red curve) in comparison to radhydro simulations (blue dots) for modest mode 2 distortions (a factor of two in shape, and of four in  $\rho r$ ). Rather than using the starting amplitude of the distortion, models were compared with the same hotspot and shell  $\rho r$  asymmetries at bang time.

matched. The correspondence between initial and final amplitude of the perturbation was less well matched. An isobaric model would tend to overpredict the growth of perturbations due to the ‘instantaneous’ aspect of the model that ignores the flow and associated delay within the hotspot. Similarly, the absence of nonradial flow would tend to underpredict the growth due to the thinning of curved flows (although these are small for low modes). Given the possible inaccuracies in the growth rate of perturbations in the model, it is important to match the observed  $\rho r$  variation at bang time. To ensure this, the 3D seeds are chosen using a growth factor analysis to match the observed  $\rho r$  variation at bang time, rather than the smaller inflight amplitudes of the perturbations.

## 6. Application of 3D model to data

The 3D model is initialized with  $\rho r$  perturbations that grow as the implosion converges and these are chosen to match the 3D asymmetry and radiative loss at stagnation. The inputs to the model are from measurements. First, the 1D parameters,

the implosion velocity, the cold fuel adiabat and the fuel and remaining (unablated) ablator mass, ( $v_{\text{imp}}$ ,  $\alpha$ ,  $M_r$ ,  $M$  respectively) are chosen for the model. These values come from models of experiments that match the shock timing, bang time and backlit convergent ablator data. Next the hotspot adiabat which determines the starting value of hotspot  $PV^\gamma$  is chosen by picking the initial hotspot energy  $E_o$  at an arbitrary mean starting radius  $R_o$ . The value of  $E_o$  corresponds approximately to the initial kinetic energy of the central DT gas vapor, which is swept up at the sum of implosion and release velocities (several times the sound speed) of the compressed cold fuel. The hotspot adiabat controls the convergence and stagnation pressure with corrections for net alpha heating, and is chosen to match the observed  $\rho r$  or down-scattered ratio (DSR)—the intensity of neutrons in the 10–12 MeV energy range relative to the total number of neutrons near 14 MeV, which is related to the fuel  $\rho r$ . Often the DSR in the experiment is smaller than that of the simulation, indicating an issue with convergence, preheat or fuel–ablator mixing. Impurities in the hotspot can cause the radiative loss to be higher than that of clean DT, and this enhancement of the radiative loss is routinely measured by comparing the 22 keV x-ray yield measured with the south pole bang time x-ray crystal monochromator to the neutron yield [20, 21]. Since both x-ray and neutron yield scale as  $P^2V\tau$ , the yield ratio  $\frac{Y_{x22\text{keV}}}{Y_n}$  is routinely used to infer the excess radiative loss due to impurities in the hotspot. The radiative loss enhancement is inferred for each shot, and values from nominal to a few tens of percent are typical. Finally, the 3D low-mode shell asymmetries are modeled by putting in a small ‘seed’ perturbation so that at stagnation and bounce the  $\rho r$  perturbations will have grown to the values observed in the 20 FNADs and the five NTOF detectors placed around the chamber. FNADs measure the uniformity of neutron scattering and are used to infer the relative  $\rho r$  asymmetry at stagnation [22]. The NTOF detectors, which determine a detailed neutron spectrum, are used to infer the absolute fuel  $\rho r$  using the intensity of the down-scattered spectrum in the 10–12 MeV range [23]. The data from FNADs and NTOF detectors only provide a ‘lower limit’ for the shell perturbations (modes 0, 1, 2) because they are insensitive to features smaller than the hotspot, such as the tent and fill tube. When needed,  $\rho r$  perturbations due to engineering features such as the tent are included in the model. The  $\rho r$  and its angular variation at stagnation are fitted to the sum of nine  $Y_{lm}$  for modes 0, 1 and 2, and these are used as input for the 3D model as a seed perturbation. Typical  $\rho r$  growth factors in the model are 50 times, and so at the starting configuration at 200  $\mu\text{m}$  radius the shape errors are only a few microns. By stagnation they grow to the measured values by construction.

While the model inputs are 1D parameters ( $v_{\text{imp}}$ ,  $\alpha$ ,  $M_{\text{fuel},r}$  and  $E_o$ ), the radiative loss enhancement and 3D seed shape, the model outputs are detailed time and angular dependent quantities describing the hotspot and shell:  $P_{\text{hs}}(t)$ ,  $T_{\text{hs}}(t)$ ,  $Q_\alpha(t)$ ,  $Q_{\text{rad}}(t)$ ,  $Q_{\text{cond}}(t)$ ,  $R_{\text{hs},s}(t, \theta, \varphi)$ . Of particular interest in the model are the burn averaged bang time quantities:  $Y_n$ ,  $T_{\text{ion}}$ ,  $\Delta\rho r(\theta, \varphi)$ ,  $R_{\text{hs}}(\theta, \varphi)$ ,  $Y_{\text{xray}}$  and RKE.

The 3D model reproduces the high yield HDC shot N170601 [24–27], using inputs from post-shot models:  $v_{\text{imp}} = 381 \text{ km s}^{-1}$ ,  $\alpha = 2.3$ ,  $M_{\text{fuel}} = 135 \mu\text{g}$ ,  $M_{\text{tot}} = 175 \mu\text{g}$ ,  $E_o = 117\text{J}$ , with  $R_o = 200 \mu\text{m}$ . While the average fuel  $\rho r$  at bang time was  $0.642 \text{ g cm}^{-2}$  the FNADs’ data show a large mode 1 component (amplitude =  $0.278 \text{ g cm}^{-2}$  with a thin region at  $\varphi \sim 90^\circ$ , which is 1.6 times thinner than average, and a thick region at  $\varphi \sim 270^\circ$  which is over twice as thick as the thin region. Figure 3 shows this example of the growth of perturbations for shot N170601, plotting an equatorial line-out of the  $\sim 1\%$  starting seed that was chosen to match the final  $\rho r$  asymmetry at bang time before velocity corrections, as discussed below. The hotspot and return shock show a significant offset from center, and the observed  $\rho r$  variation is not aligned with the hohlraum axis. This  $\rho r$  asymmetry leads to a velocity of the hotspot at bang time that resembles the modal structure of the FNADs, where thin regions are expanding and thick regions still converging. Velocities in the hotspot from the high  $\rho r$  to the low  $\rho r$  enhance the response of the FNADs’ threshold detectors which are sensitive to the bulk velocity shifts in neutron energy [28]. This reduces the amplitude of the mode 1  $\rho r$  asymmetry, typically by  $\sim 30\%$ , giving a mode 1 component of  $\rho r = 0.194 \pm 0.02 \text{ g cm}^{-2}$  and a net bulk flow velocity of  $\sim 60 \text{ km s}^{-1}$ , towards  $\varphi = 84^\circ$ ,  $\theta = 42^\circ$ . The 3D model with velocity corrections matches the performance of the high yield HDC shot N170601. Table 1 shows the individual contributions to the reduction in performance from 1D in order of importance: the 3D  $\rho r$  asymmetries, the lower DSR and the increased radiative loss. The  $\rho r$  asymmetry and lower than simulated  $\rho r$  account for the bulk of the eight-fold reduction in yield.

The dynamic model captures the 20-shot high-foot performance trends but must include a  $\Delta\rho r$  aneurysm for the tent [11, 29–33]. The data show a velocity cliff associated with a drop in stagnation pressure as velocities are pushed above  $375 \text{ km s}^{-1}$ , and coast time below 0.5 ns. As the capsules are pushed harder, their performance drops, and the highest stagnation pressure and yield were limited to  $\sim 225 \text{ GBar}$  and  $\sim 1 \times 10^{16}$  respectively. A single model was used to fit the entire shot series using a rocket model to trade off velocity and remaining mass. Because different thickness ablators and other capsule parameters were varied, we plot the inferred hotspot pressure as a function of coast time. Low coast time is associated with higher velocity and lower remaining mass, likewise longer coast time is associated with lower velocity and higher remaining mass [34]. In 1D, the dynamic model ignites at velocities higher than  $375 \text{ km s}^{-1}$  and coast times lower than 0.5 ns, and the predicted stagnation pressures are much higher than the data. If we use P2 and P4 shape errors chosen to match the typical 30% rms of the FNADs’  $\rho r$  variation, the dynamic model ignites at velocities higher than  $400 \text{ km s}^{-1}$ . The low-mode shape errors observed in the high-foot series were not sufficient to prevent ignition, and yet that model does not show the loss of stagnation pressure as the capsules are driven to high velocity, and low remaining mass. If we include a tent scar, whose angular extent was that observed in 2D Convergent Ablator (2D Con A) imaging



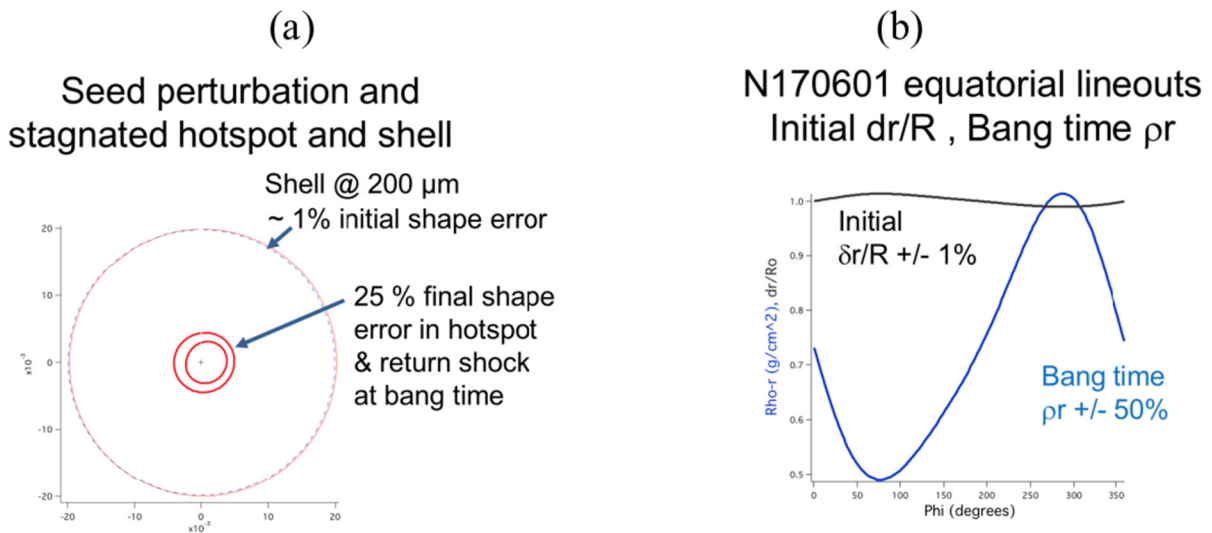


**Figure 3.** Equatorial lineouts of 3D model for HDC shot N170601 before velocity corrections. (a) A 1% initial shape error grows to 25% shape error at bang time in the hotspot and return shock. (b) The initial shape error was chosen to match the observed 50%  $\rho r$  asymmetry at bang time.

**Table 1.** Using 1D inputs for velocity, adiabat and total mass, the 3D model for N170601 matches yield and  $T_{\text{ion}}$  with degradations from observed  $\rho r$  asymmetries, with observed lower compression, and with observed increased radiative loss due from fill tube mix. Either the  $\rho r$  asymmetry or the lower than simulated  $\rho r$  account for the bulk of the eight-fold reduction in yield.

Model	DSR (%)	Yield	DT $T_{\text{ion}}$ (keV)	$P_{\text{stag}}$ (Gbar)	RKE bounce (J)
1D	3.50	$1.3 \times 10^{17}$	6.73	529	0
FNADS 3D (modes 0–2)	3.50	$2.7 \times 10^{16}$	4.97	414	12
FNADS 3D ( $E_0 + 12\%$ )	3.20	$2.0 \times 10^{16}$	4.71	354	68
FNADS 3D (radiative loss $\times 1.15$ )	3.20	$1.6 \times 10^{16}$	4.56	337	73
Experiment	3.20	$1.6 \times 10^{16}$	4.69 (DT) 4.29 D(DD)	300 est.	

experiments [35], with a mass deficit of  $20 \mu\text{g sr}^{-1}$  or  $\sim 10\%$  of initial mass  $\text{sr}^{-1}$ , which is chosen to fit the data trends, we find that as velocity is increased, and remaining mass is decreased, the tent scar becomes ineffective at confining the hotspot, and represents a dynamic leak [11]. The model matches the pressure trends for the whole series, and like the experiments, the yields were limited to  $< 1 \times 10^{16}$ . The results of the model are shown in figure 4. The 3D model shows as much as a 30–100-fold reduction in yield from the 1D models that ignite, and the tent aneurysm was the largest contribution to this degradation at high velocity. With hindsight, the tent aneurysm is the root cause of low stagnation pressure observed in the National Ignition Campaign [36].

The 3D dynamic model was applied to try to understand the stagnation pressure deficit in the direct drive DT experiment 77066 at the University of Rochester Omega laser [37]. Experimental data from this experiment were used to infer a record-setting stagnation pressure of 57 Gbar, which is significantly less than the  $\sim 100$  Gbar from simulation including known target and laser imperfections. The dynamic model for the direct drive experiment used a model with a hydro-scale factor of half that of the NIF (energies and volumes are typically  $1/8$  the NIF equivalents), velocity of  $380 \text{ km s}^{-1}$  and adiabat of 3.7, and achieved a yield of  $1.3 \times 10^{14}$  and a pressure of 101 Gbar in 1D. Because the Omega laser

is not equipped with multi-view NTOF detectors capable of inferring fuel  $\rho r$  asymmetry, nor an array of activation diagnostics to observe  $\rho r$  asymmetry at stagnation, the 3D model was constructed with measured power balance of the 60-beam overlap, including the measured  $4 \mu\text{m}$  target offset provided by Igumenshchev and Gatu-Johnson [38], and included shell  $\rho r$  asymmetry measured at shockflash, rather than bang time. The target offset for cryogenic shots with a shroud is measured to  $\sim 1 \mu\text{m}$  accuracy by comparing 15 camera views recorded on carefully aligned warm targets. The 3D dynamic model for Omega shot 77066, with as-shot 60-beam power balance and measured  $4 \mu\text{m}$  target offset, leads to  $< 2\%$  flux asymmetry peak-to-valley. This degree of flux asymmetry leads to a stagnation  $\rho r$  asymmetry shown in figure 5, and results in only a small decrease in stagnation pressure (101 Gbar  $\rightarrow$  98 Gbar) rather than the 57 Gbar inferred from data.

Next, a model for the spatially dependent pattern of the cross beam energy transfer (CBET) was created using the 60-beam overlap patterns, and then used to create the perturbations at modes 10–18 that one could expect from CBET [39]. When this was applied, it created multiple mode 10 jets that entered the hotspot, and tended to reduce the size of the hotspot and drop the temperature. The amplitude of the mode 10–18 CBET perturbations was limited to that supported by

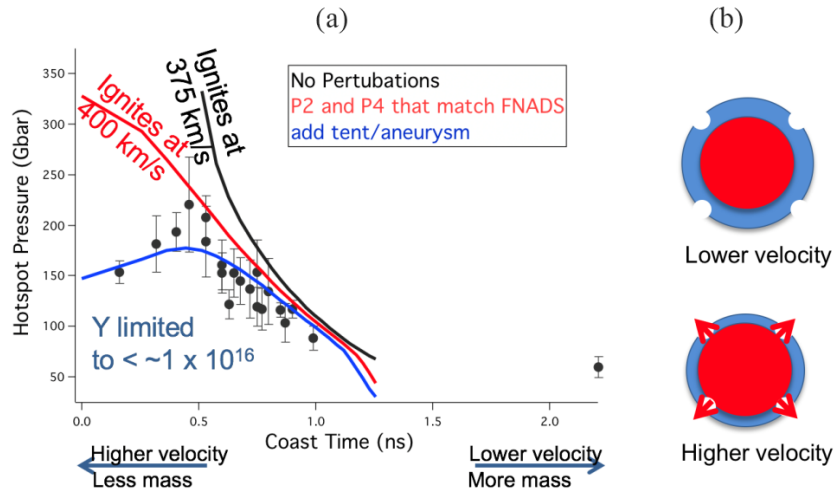


**Figure 4.** (a) The inferred stagnation pressure for the 20-shot high-foot series is plotted versus coast time. A dynamic model uses a rocket equation to trade mass and velocity and is plotted: with no perturbation (black), with P2 and P4  $\rho r$  asymmetry matching the 30% rms variation seen in FNADs (red), and with additional tent aneurysm (blue) which causes a velocity cliff and yield to be limited to  $\leq 1 \times 10^{16}$ . (b) An illustration explaining tent aneurysm that is most important at high velocity when remaining mass is insufficient to tamp the tent region. The mass deficit is chosen to match stagnation data.

### Beam balance, target offset, (and CBET) lead to only modest rho-r asymmetry

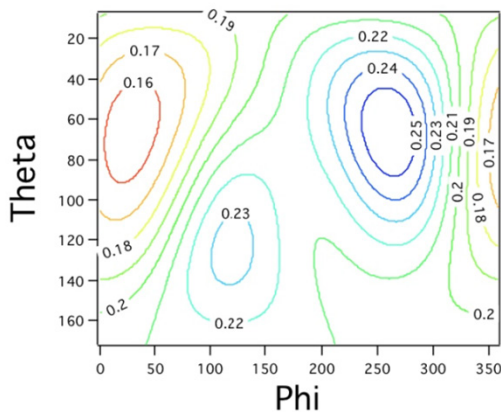


**Figure 5.** The 3D dynamic model for Omega shot 77066 was constructed using the as-shot 60-beam power balance and measured  $4 \mu\text{m}$  target offset, which leads to  $<2\%$  flux asymmetry peak-to-valley. This degree of flux asymmetry leads to a stagnation  $\rho r$  asymmetry as shown in the plot, and only a small decrease in stagnation pressure (101 Gbar  $\rightarrow$  98 Gbar), rather than the 57 Gbar inferred from data.

the measured  $21.5 \mu\text{m}$  hotspot radius. This resulted in only a modest impact on yield and stagnation pressure as indicated in table 2. The result of this study was that the beam balance, target offset and mode 10–18 CBET were five times smaller than those needed to match stagnation data.

Finally, a model was constructed that examined a possible  $\rho r$  deficit associated with the mounting stalk and glue fillet. This model used  $D^3\text{He}-p$  proton data provided by Gatu-Johnson [40] that inferred a  $\sim 25\%$  drop in shell  $\rho r$  at angles within  $40^\circ$  of the stalk at shockflash, when the shell  $\rho r$  was ten times smaller than at stagnation. When such an early time  $\rho r$  perturbation is included in the dynamic model, there is a significant drop in resulting stagnation pressure and yield,

**Table 2.** A table showing yield and stagnation pressure from a study of shot 77066 using the 3D dynamic model. Models for 60-beam power balance and target offset do not produce sufficient low-mode asymmetry to explain observed data; they are five times too small. Including CBET perturbations at the amount limited by observed hotspot size gives a small drop in yield and stagnation pressure. Including a  $\rho r$  defect associated with the stalk inferred from  $D^3\text{He}-p$  proton data would explain the observed yield and pressure drop in the data, but is not consistent with radiography data, therefore requiring additional data to resolve differences.

Shot 77066	Yield	Pressure (Gbar)
1D	$1.3 \times 10^{14}$	101
Balance/offset	$1.2 \times 10^{14}$	98
BB + CBET	$1.1 \times 10^{14}$	95
Experiment	$0.4 \times 10^{14}$	57
BB + Stalk	$0.4 \times 10^{14}$	57

down to the observed values as indicated in table 2. This result hinges on an inference of a  $\rho r$  defect caused by the stock which is observed at shockflash from  $D^3\text{He}-p$  proton data on another shot, and is predicted by the 3D model to significantly impact performance of DT layered implosions. Radiography data from Stoeckl [41], however, show that by bang time the perturbation due to the stock may have reassembled, although it is not clear if it would have effectively contained the hotspot pressure in the process. Additional data are needed to resolve these issues.

### 7. A proposed 3D ignition criterion

We have extended the 3D model to make predictions of performance as we push targets to higher yield. For example, we could ask of the model what would happen if we push the HDC targets to higher velocity given their observed performance based on the  $\rho r$  and asymmetries. What we find is a velocity cliff, where as we push to higher velocity, the  $\rho r$

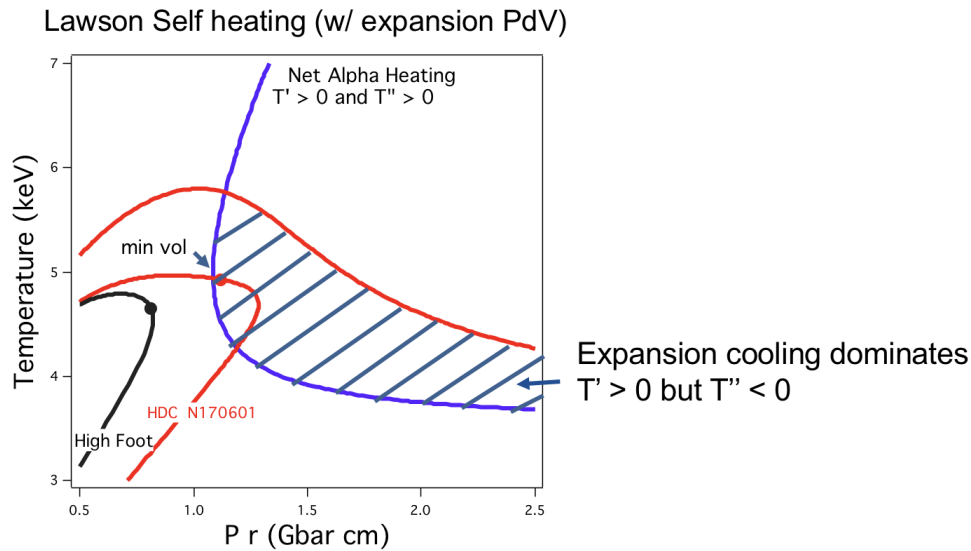


**Figure 6.** A modified Lawson diagram for ignition. In 1D without expansion we recover the familiar Lawson self-heating curve (blue) which is the boundary of self-heating  $\frac{dT}{dt} > 0$ . The cross-hatched region denotes a fizzle region for N170601 that is dominated by expansion cooling, given observed  $\rho r$  and asymmetry. This region is characterized by  $\frac{d^2T}{dt^2} < 0$  near minimum volume. Also shown are trajectories for the best high-foot shot (black) and the high yield HDC N170601 (red). While the HDC implosions enter the self-heating regime, hydro-disassembly would require the temperature to exceed  $\sim 5.5$  keV for ignition to occur.

perturbations increase and the remaining mass decreases until the minimum  $\rho r$  is too low to confine the hotspot. The model predicts modest improvement with velocity, and a ‘velocity cliff’, similar to that observed with the high-foot series. During compression before the hotspot reaches minimum volume, the  $PdV$  work is beneficial in increasing both hotspot temperature and pressure. During expansion, the  $PdV$  work tends to decrease the pressure, temperature and reaction rates, and the rate of expansion cooling increases linearly in time near minimum volume. To achieve ignition, it is important that the net alpha heating be both positive and also increasing faster than the rate of  $PdV$  expansion. This is equivalent to requiring that both  $\frac{dT}{dt} > 0$  and  $\frac{d^2T}{dt^2} > 0$  at minimum volume.

The rate of  $PdV$  expansion can be estimated by expanding about the minimum volume

$$V \sim V_{\min} + \frac{1}{2} \frac{d^2V}{dt^2} (t - t_{\min})^2 \text{ and } \frac{dV}{dt} \sim \frac{d^2V}{dt^2} (t - t_{\min}). \quad (31)$$

$$\frac{dT}{dt} = \frac{T}{E_{\text{hs}}} (f_{\alpha} Q_{\alpha} - Q_{\text{rad}} - Q_{\text{cond}}) - \frac{2}{3} \frac{T}{V} \frac{d^2V}{dt^2} (t - t_{\min}) > 0. \quad (32)$$

The first term on the right-hand side of equation (32) is the familiar Lawson curve for self-heating without expansion,  $\frac{dT}{dt} > 0$  at minimum volume without any  $PdV$  work. The second term represents the expansion cooling which increases linearly in time from minimum volume. To ensure that the net heating continues beyond minimum volume we require the second derivative of temperature to be positive around minimum volume

$$\frac{d^2T}{dt^2} = \frac{d^2T_{\text{static}}}{dt^2} - \frac{2}{3} \frac{T}{V} \frac{d^2V}{dt^2} > 0 \quad (33)$$

where

### Lawson Self heating (w/ expansion PdV)

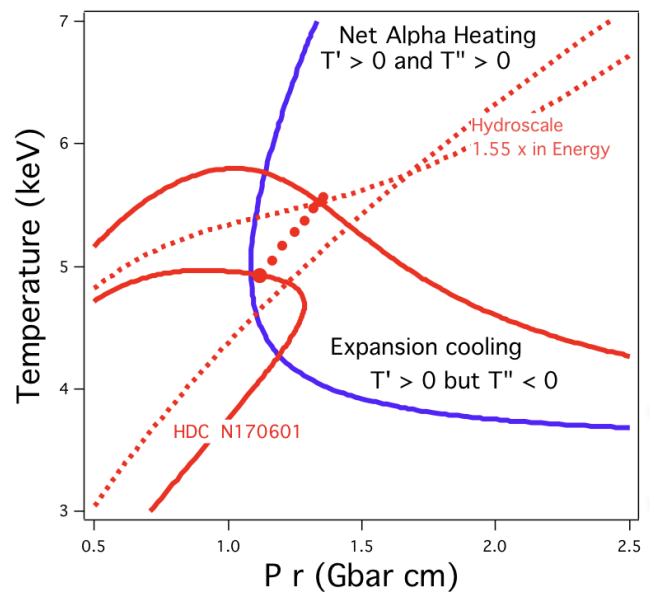


**Figure 7.** A plot similar to figure 6 but showing the expected hydro-scaling of N170601 for energy scaling factors 1.0 to 1.6 in steps of 0.1. The minimum volume conditions (red dots) improve with scale factor, and ignition occurs outside the expansion cooling regime at temperatures above 5.5 keV.

$$\frac{dT_{\text{static}}}{dt} = \dot{T}_{\text{static}} = \frac{T}{E_{\text{hs}}} (f_{\alpha} Q_{\alpha} - Q_{\text{rad}} - Q_{\text{cond}}) \text{ and } \frac{dP_{\text{static}}}{dt} = \frac{P}{E_{\text{hs}}} (Q_{\alpha} - Q_{\text{rad}}) \quad (34)$$

are the dependence of temperature and pressure at minimum volume without  $PdV$  work. We obtain a condition on the pressure and temperature at minimum volume needed to ensure

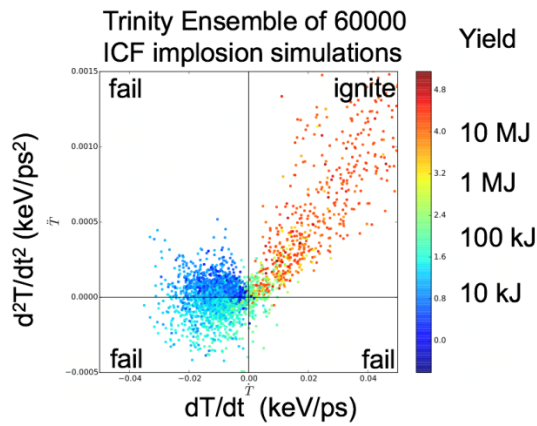


**Figure 8.** A scatter plot of yield (color) versus  $\frac{dT}{dt}$  and  $\frac{d^2T}{dt^2}$  at minimum volume for an ensemble of 60 000 2D ICF implosion simulations performed at the Trinity supercomputer.

that the second derivative of temperature will remain positive during expansion

$$\frac{d^2T_{\text{static}}}{dt^2} = \frac{dT_{\text{static}}}{dT} \frac{dT_{\text{static}}}{dt} + \frac{dT_{\text{static}}}{dP} \frac{dP_{\text{static}}}{dt} > \frac{2}{3} \frac{T}{V} \frac{d^2V}{dt^2}. \quad (35)$$

This expression is evaluated numerically using the known dependence of the terms on pressure and temperature, and the expected time dependence of pressure and temperature at minimum volume. The dependence on 3D disassembly is in the term  $\frac{2}{3V} \frac{d^2V}{dt^2}$ , which is dominated by the acceleration of the hotspot providing the RKE is small  $\frac{d^2V}{dt^2} \sim \int r_{\text{hs}}^2 \ddot{r}_{\text{hs}} d\Omega$  with  $\ddot{r}_{\text{hs}} \sim \frac{(P_{\text{hs}} - P_s)}{\rho r} = \frac{(P_{\text{hs}} - P_s) 4\pi r^2}{m}$ , and depends on the 3D morphology because of its dependence on the large radius, thin regions of the shell.

Figure 6 shows the ignition regime for N170601. In 1D without expansion we recover the familiar Lawson self-heating curve (blue) which is the boundary of self-heating  $\frac{dT}{dt} > 0$ . The cross-hatched region denotes a fizzle region for N170601 that is dominated by expansion cooling given the observed  $\rho r$  and asymmetry. This region is characterized by  $\frac{d^2T}{dt^2} < 0$  at minimum volume, where a value of  $\frac{\dot{V}}{V} = 5 \times 10^{20} \text{ s}^{-2}$  is used to estimate the volume expansion as quadratic over the required time. Also shown are trajectories for the best high-foot shot (black) and the high yield HDC N170601 (red). While the HDC implosions enter the self-heating regime, the hydro-disassembly would require the temperature to exceed  $\sim 5.5 \text{ keV}$  for ignition to occur. Figure 7 shows the result of hydro-scaling of N170601, which would require an increase by a factor of 1.6 in capsule energy to reach ignition conditions, and also shows that this does not occur until temperatures at minimum volume exceed  $5.5 \text{ keV}$ . Finally, the requirements  $\frac{dT}{dt} > 0$  and  $\frac{d^2T}{dt^2} > 0$  were examined in a subset of the ensemble of 60 000 2D ICF implosion simulations at the LANL Trinity supercomputer [42, 43] and are plotted in figure 8. Generally, simulations with both  $\frac{dT}{dt}$  and  $\frac{d^2T}{dt^2} > 0$  ignited, and simulations with either  $\frac{dT}{dt}$  or  $\frac{d^2T}{dt^2} < 0$  failed to ignite. All NIF shots examined failed in the quadrant where  $\frac{dT}{dt} > 0$  but  $\frac{d^2T}{dt^2} < 0$ , which is under-sampled

in the simulations, that did not include tent defects or 3D asymmetry. High resolution 3D simulations of the ignition boundary are planned, but are beyond the scope of current capability, which will start with low-mode 3D simulations in the next year.

## 8. Conclusion

A simple 3D dynamic model for ICF implosions has been developed and used to assess the impacts of low-mode asymmetry, aneurysms and mix-induced radiative loss on capsule performance across ICF platforms. Experimental data are used as input to seed 3D perturbations in the model so that the actual observed hotspot and shell  $\rho r$  asymmetry at stagnation, as well as the radiation loss increase from mix impurities, are accurately reproduced. This model is applied to a broad set of implosion data, matches most experimental observables and explains major performance degradation mechanisms, which can be as large as factors of 30–100 in yield. We also examine a modified ignition criterion that accounts for increase in the expansion  $PdV$  work due to the presence of 3D  $\rho r$  perturbations and loss-of-confinement in thin regions of the shell.

## Acknowledgments

Work performed under the auspices of the United States Department of Energy by Lawrence Livermore National Laboratory under contract DE-AC52-07NA273.

## Disclaimer

This document was prepared as an account of work sponsored by an agency of the United States government. Neither the United States government nor Lawrence Livermore National Security, LLC, nor any of their employees makes any warranty, expressed or implied, or assumes any legal liability or responsibility for the accuracy, completeness, or usefulness of any information, apparatus, product, or process disclosed, or represents that its use would not infringe privately owned rights. Reference herein to any specific commercial product, process, or service by trade name, trademark, manufacturer, or otherwise does not necessarily constitute or imply its endorsement, recommendation, or favoring by the United States government or Lawrence Livermore National Security, LLC. The views and opinions of authors expressed herein do not necessarily state or reflect those of the United States government or Lawrence Livermore National Security, LLC, and shall not be used for advertising or product endorsement purposes.

## ORCID iDs

O.A. Hurricane <https://orcid.org/0000-0002-8600-5448>  
 J.E. Field <https://orcid.org/0000-0002-6082-0233>  
 J. Frenje <https://orcid.org/0000-0001-6846-0378>  
 L. Berzak Hopkins <https://orcid.org/0000-0002-9187-5667>  
 D.H. Munro <https://orcid.org/0000-0002-0662-6923>

H. Rinderknecht  <https://orcid.org/0000-0003-4969-5571>

## References

- [1] Nuckolls J., Thiessen A., Wood L. and Zimmerman G. 1972 Laser compression of matter to super-high densities—thermonuclear (CTR) applications *Nature* **239** 139–42
- [2] Edwards M.J. et al 2011 The experimental plan for cryogenic layered target implosions on the National Ignition Facility—The inertial confinement approach to fusion *Phys. Plasmas* **18** 151003
- [3] Lindl J.D. et al 2014 Review of the National Ignition Campaign 2009–2012 *Phys. Plasmas* **21** 020501
- [4] Betti R. and Hurricane O.A. 2016 Inertial-confinement fusion with lasers *Nat. Phys.* **12** 435–48
- [5] Betti R. et al 2015 Alpha heating and burning plasmas in inertial confinement fusion *Phys. Rev. Lett.* **114** 1–5
- [6] Edwards M.J. et al 2013 Progress towards ignition on the National Ignition Facility *Phys. Plasmas* **20** 1–10
- [7] Clark D.S. et al 2016 Three-dimensional simulations of low foot and high foot implosion experiments on the National Ignition Facility *Phys. Plasmas* **23**
- [8] Weber C.R. et al 2015 Three-dimensional hydrodynamics of the deceleration stage in inertial confinement fusion *Phys. Plasmas* **22**
- [9] Kritcher A.L. et al 2016 Integrated modeling of cryogenic layered highfoot experiments at the NIF *Phys. Plasmas* **23**
- [10] Tommasini R. et al 2015 Tent-induced perturbations on areal density of implosions at the National Ignition Facility *Phys. Plasmas* **22**
- [11] Hurricane O.A. et al 2016 Inertially confined fusion plasmas dominated by alpha-particle self-heating *Nat. Phys.* **12** 800–6
- [12] Spears B.K. et al 2014 Mode 1 drive asymmetry in inertial confinement fusion implosions on the National Ignition Facility *Phys. Plasmas* **21**
- [13] Rosen M. and Szoke A. 2015 private communication
- [14] Betti R. et al 2002 Deceleration phase of inertial confinement fusion implosions *Phys. Plasmas* **9** 2277–86
- [15] Caughlan G.R. and Fowler W.A. 1988 Thermonuclear reaction rates 5 *At. Data Nucl. Data Tables* **40** 283–334
- [16] Krokhin O.N. and Rozanov V.B. 1973 Escape of alpha particles from a laser-pulse-initiated thermonuclear reaction *Sov. J. Quantum Electron.* **2** 393–4
- [17] Scott H.A. and Hansen S.B. 2010 Advances in NLTE modeling for integrated simulations *High Energy Density Phys.* **6** 39–47
- [18] Kemp A., Meyer-ter-Vehn J. and Atzeni S. 2001 Stagnation pressure of imploding shells and ignition energy scaling of inertial confinement fusion targets *Phys. Rev. Lett.* **86** 3336–9
- [19] Kritcher A.L. et al 2014 Metrics for long wavelength asymmetries in inertial confinement fusion implosions on the National Ignition Facility *Phys. Plasmas* **21**
- [20] Ma T. et al 2013 Onset of hydrodynamic mix in high-velocity, highly compressed inertial confinement fusion implosions *Phys. Rev. Lett.* **111**
- [21] Ma T. et al 2017 The role of hot spot mix in the low-foot and high-foot implosions on the NIF *Phys. Plasmas* **24** 056311
- [22] Yeamans C.B. and Bleuel D.L. 2017 The spatially distributed neutron activation diagnostic FNADs at the National Ignition Facility *Fusion Sci. Technol.* **72** 120–8
- [23] Glebov V.Y. et al 2006 Development of nuclear diagnostics for the National Ignition Facility (invited) *Rev. Sci. Instrum.* **77**
- [24] Ho D.D. et al 2016 Implosion configurations for robust ignition using high-density carbon (diamond) ablator for indirect-drive ICF at the National Ignition Facility *J. Phys.: Conf. Ser.* **717**
- [25] Hopkins L.F.B. et al 2015 First high-convergence cryogenic implosion in a near-vacuum hohlraum *Phys. Rev. Lett.* **114**
- [26] Hopkins L.F.B. et al 2015 Near-vacuum hohlraums for driving fusion implosions with high density carbon ablaters *Phys. Plasmas* **22** 056318
- [27] Le Pape S. et al 2018 Fusion energy output greater than the kinetic energy of an imploding shell at the National Ignition Facility *Phys. Rev. Lett.* **120**
- [28] Rinderknecht H.G., Bionta R., Grim G., Hatarik R., Khater H., Schlossberg D. and Yeamans C. 2018 Velocity correction for nuclear activation detectors at the NIF *Rev. Sci. Instrum.* **89**
- [29] Park H.S. et al 2014 High-adiabat high-foot inertial confinement fusion implosion experiments on the national ignition facility *Phys. Rev. Lett.* **112** 055001
- [30] Callahan D.A. et al 2015 Higher velocity, high-foot implosions on the National Ignition Facility laser *Phys. Plasmas* **22**
- [31] Hinkel D.E. et al 2016 Development of improved radiation drive environment for high foot implosions at the National Ignition Facility *Phys. Rev. Lett.* **117**
- [32] Ma T. et al 2015 Thin shell, high velocity inertial confinement fusion implosions on the National Ignition Facility *Phys. Rev. Lett.* **114** 145004
- [33] Doeppner T. et al 2015 Demonstration of high performance in layered deuterium–tritium capsule implosions in uranium hohlraums at the National Ignition Facility *Phys. Rev. Lett.* **115** 055001
- [34] Hurricane O.A. et al 2017 On the importance of minimizing ‘coast-time’ in x-ray driven inertially confined fusion implosions *Phys. Plasmas* **24**
- [35] Rygg J.R. et al 2014 2D x-ray radiography of imploding capsules at the National Ignition Facility *Phys. Rev. Lett.* **112**
- [36] Cerjan C., Springer P.T. and Sepke S.M. 2013 Integrated diagnostic analysis of inertial confinement fusion capsule performance *Phys. Plasmas* **20**
- [37] Regan S.P. et al 2016 Demonstration of fuel hot-spot pressure in excess of 50 Gbar for direct-drive, layered deuterium–tritium implosions on OMEGA *Phys. Rev. Lett.* **117**
- [38] Gatu-Johnson M. and Igumenshchev I.V. 2017 private communication
- [39] Igumenshchev I.V. et al 2017 Three-dimensional hydrodynamic simulations of OMEGA implosions *Phys. Plasmas* **24**
- [40] Gatu-Johnson M. et al 2018 Impact of asymmetries on fuel performance in inertial confinement fusion *Phys. Rev. E* **98** 051201
- [41] Stoeckl C. et al 2017 Monochromatic backlighting of direct-drive cryogenic DT implosions on OMEGA *Phys. Plasmas* **24**
- [42] Nora R., Peterson J.L., Spears B.K., Field J.E. and Brandon S. 2017 Ensemble simulations of inertial confinement fusion implosions *Stat. Anal. Data Min.* **10**
- [43] Peterson J.L. et al 2017 Zonal flow generation in inertial confinement fusion implosions *Phys. Plasmas* **24** 032702